Two-dimensional action spectroscopy of excitonic systems

Explicit simulation using a phase-modulation technique

Damtie, Fikeraddis A.; Wacker, Andreas; Pullerits, Tõnu; Karki, Khadga J.

Published in:
Physical Review A

DOI:
10.1103/PhysRevA.96.053830

2017

Document Version:
Publisher's PDF, also known as Version of record

Two-dimensional action spectroscopy of excitonic systems: Explicit simulation using a phase-modulation technique

Fikeraddis A. Damtie[*] and Andreas Wacker[†]
Mathematical Physics and NanoLund, Lund University, Box 118, 22100 Lund, Sweden

Tõnu Pullerits[‡] and Khadga J. Karki[§]
Chemical Physics and NanoLund, Lund University, Box 124, 22100 Lund, Sweden
(Received 18 July 2017; published 13 November 2017)

Two-dimensional (2D) spectroscopy has been intensively used to study electronic and vibronic coherences in biological systems and semiconductors. This technique studies coherent as well as incoherent signals that arise from the nonlinear interaction of a sequence of laser pulses. In this paper we present a direct evaluation of the 2D signal based on elementary quantum kinetics in order to compare with the common approximate diagrammatic approaches. Here we consider incoherent action signals such as fluorescence or photocurrent as the observable, which is easily accessible in a measurement. These observables are calculated by solving the time evolution of the density matrix in the Lindblad form, which can take into account all possible decoherence processes. The phase modulation technique is used to separate the relevant nonlinear signals from the other possible interaction pathways. The approach can be used to calculate 2D spectra of any quantum system. For our model system we find a good agreement for the quantum beating between the coupled states.

DOI: 10.1103/PhysRevA.96.053830

I. INTRODUCTION

Over the past years 2D optical spectroscopy has proven to be an efficient technique to provide an optimal information for studying the effect of optical fields on quantum systems [1–10]. Due to its ability to directly observe coherences between quantum states and to monitor the dynamics of energy transfer via changes in a 2D map, the technique has been preferred to study quantum dynamics in many systems. Among the most studied are the energy transfer mechanism in photosynthetic light harvesting systems [11,12], and ultrafast dynamics in semiconductor nanostructures [13–15]. Particularly, the origin of beating signals in 2D spectra observed in mixed vibronic systems has been recently debated in literature [16–20].

Signals for 2D spectroscopy can be obtained via different techniques. Most commonly three noncollinear pulses are used in which the pulses interact with the system to generate a coherent response due to third-order polarization in a specified wave-vector matched direction [21–25]. The method is often called photon echo 2D spectroscopy (PE2D). Phase cycling has also been used to isolate nonlinear signals relevant for 2D spectroscopy [26–29]. In yet another technique, one uses four collinear pulses with well defined phases and detects the excited state populations as incoherent action signals, such as fluorescence or photocurrent. This technique may be called as action signal detected 2D spectroscopy based on phase modulation [15,25,30–36]. All the approaches provide equivalent signals for the different pathways in the nonlinear light-matter interactions [32].

One of the advantages of using incoherent action detection is that the signals from small volumes, such as a single molecule or a quantum dot, can be used for the spectroscopy. Generation of the coherent signals in a spatially isolated phase matched direction, on the other hand, requires the sample size to be larger than the wavelength of the incident light field [1,6]. On the computational side, the action signals can be easily calculated by following the total relaxation from the associated excited states, and the signals that are relevant for the 2D spectroscopy can be separated from the other linear and nonlinear signals by using the technique of phase modulation, as it is done in the experiments [15,32,34,35,37]. Moreover, unlike in the experiments where only the combined contributions from the different excited states on the action signals can be measured, the simulations can be used to disentangle the contributions from the individual excited states on the action signals.

In this work we present a method to simulate 2D spectra of an electronic system resembling an excitonic dimer based on the phase modulation technique. Previously, simulation of 2D spectra based on the explicit calculations of the nonlinear coherent response from an ensemble of systems have been carried out [38,39]. However, such calculations cannot be used to simulate 2D spectra from a single excitonic system. Others have used analytical response function of the nonlinear action signals that result from selected pathways in the Feynman diagrams [32]. Vela *et al.* [35] have used a three-level model to simulate the photocurrent detected 2D spectra by using the Lindblad master equation. Here we simulate the full interaction of a sequence of four laser pulses with a model system containing four energy levels. The model is equivalent to two excitonically coupled molecules each having two levels. However, the approach is general and any system with analogous energy level structure and the corresponding optical transitions can be modeled. We calculate processes associated with all different relaxation pathways by solving the time evolution of the density matrix in the Lindblad form, which

[*]Fikeraddis.Damtie@teorfys.lu.se
[†]Andreas.Wacker@fysik.lu.se
[‡]Tonu.Pullerits@chemphys.lu.se
[§]Khadga.Karki@chemphys.lu.se

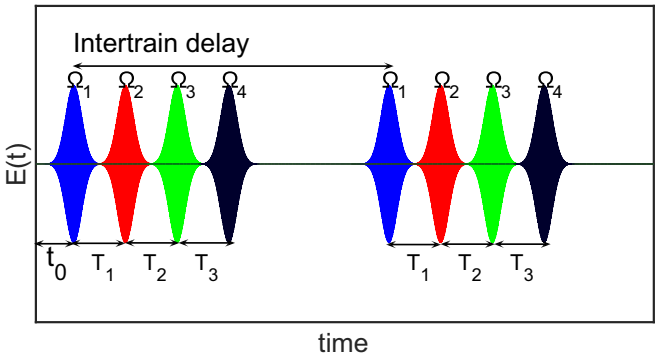

FIG. 1. Pulse sequences used in the simulation as a function of time. Interpulse delays and intertrain delays are indicated. The first two trains of pulses are shown.

takes into account decoherence processes. Compared to the previous works, we analyze action signals associated with all the excited states, which also incorporate all the pathways, namely the ground state bleach (GSB), stimulated emission (SE), and excited state absorption (ESA), that contribute to a 2D signal. We investigate in detail the evolution of the diagonal and the cross peaks in the 2D spectra as a function of population time, which reveal transfer of population and coherences between the different states. The spectra also show coherent beatings of the peaks at the frequency that matches the energy splitting between the excitons. Moreover, our methodology allows us to investigate the evolution of the double quantum coherence (DQC) spectra [40]. Our analysis shows that the DQC spectra reveal the dephasing dynamics of the high lying excited state, which could play an important role in the investigation of thermal relaxation of hot excited states in metals and semiconductors.

In addition to the four-level system considered, this method can be used to study more complicated systems, which involve large number of excitations. One such scenario can be the study of multiple exciton generation (MEG) in nanocrystal quantum dots for applications in quantum dot based solar cells.

II. METHOD

A. Action signal detected 2D photocurrent spectroscopy with phase modulation

After excitation by a sequence of ultrashort laser pulses the different properties of a quantum system can be studied by plotting the signal as a function of excitation and detection frequency in the resulting 2D plot. In this work we employ 2D spectroscopy based on the phase modulation technique. A detailed description of the method is given in Ref. [32]. In this technique, a train of four pulses are used, where each train is separated by an intertrain delay T. Within each train the four pulses are separated by interpulse time delays T_1, T_2, and T_3, where all the delay times are positive, as shown in Fig. 1. The total electric field for the mth pulse train is defined as

$$E^m(t) = E_1^m(t) + E_2^m(t) + E_3^m(t) + E_4^m(t), \qquad (1)$$

where m counts the number of repetition and each pulse within the pulse train is described as

$$\begin{aligned}
E_1^m(t) &= E_{01}^m \exp\left(\frac{-4\ln 2(t - t_0 - mT)^2}{\tau_1^2}\right) \\
&\quad \times \cos[\omega(t - t_0 - mT) + 2\pi\Omega_1 mT], \\
E_2^m(t) &= E_{02}^m \exp\left(\frac{-4\ln 2(t - t_0 - \mathcal{T}_1 - mT)^2}{\tau_2^2}\right) \\
&\quad \times \cos[\omega(t - t_0 - \mathcal{T}_1 - mT) + 2\pi\Omega_2 mT], \\
E_3^m(t) &= E_{03}^m \exp\left(\frac{-4\ln 2(t - t_0 - \mathcal{T}_2 - mT)^2}{\tau_3^2}\right) \\
&\quad \times \cos[\omega(t - t_0 - \mathcal{T}_2 - mT) + 2\pi\Omega_3 mT], \\
E_4^m(t) &= E_{04}^m \exp\left(\frac{-4\ln 2(t - t_0 - \mathcal{T}_3 - mT)^2}{\tau_4^2}\right) \\
&\quad \times \cos[\omega(t - t_0 - \mathcal{T}_3 - mT) + 2\pi\Omega_4 mT], \qquad (2)
\end{aligned}$$

where τ represents the pulse duration and

$$\mathcal{T}_1 = T_1, \quad \mathcal{T}_2 = T_1 + T_2, \quad \mathcal{T}_3 = T_1 + T_2 + T_3.$$

In Eq. (2), t_0 is the the center of the first pulse and Ω_1, Ω_2, Ω_3 and Ω_4 are the modulation frequencies corresponding to the pulses 1 to 4, respectively. In our simulation we use a specific set of modulation frequencies: $\Omega_1 = 51.4$ MHz, $\Omega_2 = 51.9$ MHz, $\Omega_3 = 54.2$ MHz, and $\Omega_4 = 55$ MHz. These correspond to the radio frequencies used to drive the acousto-optic modulators in typical experiments [32,33]. In addition, an intertrain delay $T = 14$ ns is used, which is a typical repetition time of the laser pulses generated by an oscillator.

In practice a train of four collinear pulses can be created by splitting the output of a mode-locked oscillator using two Mach-Zehnder interferometers. An acousto-optic Bragg cell placed within each arm of the interferometers can be used to create a continuously varying phase shift to each of the four pulses [33].

When exciting a quantum system by a train with relative phase modulation at frequency ($\Omega_{21} = \Omega_2 - \Omega_1$) the resulting excited state population contains an interference contribution with a phase, which is also modulated at Ω_{21} [36,37]. The modulation in the populations manifest in the corresponding action signals, which can be separated from the rest of the signal. Usually in the experiments, only the pulses within a pair (pair 1: pulse 1 and 2, and pair 2: pulse 3 and 4) are phase locked. Thus, the four pulse train contains two independently phase-modulated pulse pairs at frequencies Ω_{21} and Ω_{43} [32,33]. In the simulations, we can easily lock the phases between all the pulses, thereby producing all the modulations in the linear signal that arise from the possible linear combinations of the modulation frequencies $\Omega_{ij} = \Omega_i - \Omega_j$. Nonlinear interference contributions, which arise due to the optical nonlinearities of the system produce signal components at all the possible combinations $\pm\Omega_1 \pm \Omega_2 \pm \Omega_3 \pm \Omega_4$. Out of all the modulations that arise from the nonlinear interactions, two of the modulation frequencies $\Omega_{43} + \Omega_{21} = 1300$ kHz

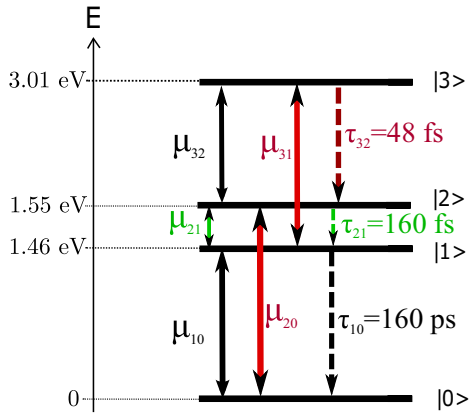

FIG. 2. Energy level diagram for the excitonic system considered in the simulation. The dipole transitions are indicated by solid double sided arrow while the relaxations are indicated by a dashed one sided arrow. Relaxation corresponds to the action that has measurable effects on signals such as light emission, photoelectron emission, or photocurrent.

and $\Omega_{43} - \Omega_{21} = 300$ kHz, which are also called the sum and difference frequencies, are important for 2D spectroscopy. These "sum" and "difference" frequency signals arise from the rephasing and nonrephasing pathways associated with the third order polarizations, respectively [32]. One of the advantages of locking all the modulation frequencies is that other important signals, such as the signal at $\Omega_4 + \Omega_3 - \Omega_2 - \Omega_1$, which is related to the DQC [40], is also readily available for investigation.

III. EVALUATION OF OBSERVABLES

A. Model

As shown in Fig. 2, we use a system with ground state $|0\rangle$, two closely lying excited states $|1\rangle$ and $|2\rangle$, and a fourth state $|3\rangle$ with energy approximately twice that of the $|1\rangle$ and $|2\rangle$. In case of an excitonic dimer, one can think of the two closely spaced excited states as single excitons and the fourth state as a double exciton.

The allowed dipole transitions are shown by the solid double arrows, which are assumed to be the same in this case. The product of the dipole matrix elements with the field amplitude is adjusted such that the maximum population transfer at zero time delay (overlapping pulses) is less than 10%. The following parameters are assumed in all the simulations. Level energies

$$E_0 = 0, \quad E_1 = 1.46\,\text{eV}, \\ E_2 = 1.55\,\text{eV}, \quad E_3 = E_1 + E_2. \tag{3}$$

Furthermore, we use the relaxation processes indicated in Fig. 2 as well as a pure dephasing rate of 100 fs for all levels. The pulse parameters used in the simulations are

$$\tau_1 = \tau_2 = \tau_3 = \tau_4 = 10\,\text{fs}, \quad \hbar\omega_{\text{pulse}} = 1.5\,\text{eV}. \tag{4}$$

B. Equation of motion for the density matrix

We model the time evolution of the reduced density operator for the system by the Lindblad equation [41]:

$$\hbar\frac{d}{dt}\hat{\rho}_S(t) = i[\hat{\rho}_S(t), \hat{H}_{\text{eff}}(t)] + \sum_{j=1}^{N_{\text{jump}}}\Gamma_j \\ \times\left\{\hat{L}_j\hat{\rho}_S(t)\hat{L}_j^\dagger - \frac{1}{2}[\hat{\rho}_S(t)\hat{L}_j^\dagger\hat{L}_j + \hat{L}_j^\dagger\hat{L}_j\hat{\rho}_S(t)]\right\}, \tag{5}$$

where the Hamiltonian H_{eff} is a sum of the time independent Hamiltonian H_0, and the interaction Hamiltonian $H_I(t)$,

$$H_{\text{eff}} = H_0 + H_I(t), \tag{6}$$

where

$$H_I(t) = -\mu E^m(t). \tag{7}$$

In Eq. (7), μ is the electric dipole transition matrix, and $E^m(t)$ is the electric field for the mth train of pulses given in Eq. (2). Throughout this paper, we use $eE_{0n}^m\mu_{ij} = 8$ meV for transitions between the allowed levels $\{i,j\}$, as shown in Fig. 2, due to the individual pulses n,m. The jump operators $\hat{L}_j$ describe different dissipation processes (with rate $\Gamma_j/\hbar$). For the model system we consider:

Relaxation from $|1\rangle \rightarrow |0\rangle$

$$\hat{L}_{\text{rel}}(1) = \hat{a}_0^\dagger\hat{a}_1 \quad \text{with strength} \quad \Gamma_{10} = 4.13\ \mu\text{eV}. \tag{8}$$

Relaxation from $|2\rangle \rightarrow |1\rangle$

$$\hat{L}_{\text{rel}}(2) = \hat{a}_1^\dagger\hat{a}_2 \quad \text{with strength} \quad \Gamma_{21} = 4.13\ \text{meV}. \tag{9}$$

Relaxation from $|3\rangle \rightarrow |2\rangle$

$$\hat{L}_{\text{rel}}(3) = \hat{a}_2^\dagger\hat{a}_3 \quad \text{with strength} \quad \Gamma_{32} = 13.78\ \text{meV}. \tag{10}$$

Dephasing in all the levels, $\hat{L}_{\text{deph}} = \hat{a}_0^\dagger\hat{a}_0$, $\hat{L}_{\text{deph}} = \hat{a}_1^\dagger\hat{a}_1$, $\hat{L}_{\text{deph}} = \hat{a}_2^\dagger\hat{a}_2$, and $\hat{L}_{\text{deph}} = \hat{a}_3^\dagger\hat{a}_3$, have the same strength $\Gamma_{\text{Dephasing}} = 41.3$ meV.

The time evolution for the density matrix is solved numerically in the Lindblad form as in Eq. (5) with the initial condition that at time zero all the population is in the ground state. The signals for constructing the 2D maps are obtained by evaluating the time integrated relaxation events given by

$$\text{Rel(t)} = \Gamma_{\text{Relaxation}}\text{Tr}\{\hat{L}_{\text{rel}}\hat{\rho}_S(t)\hat{L}_{\text{rel}}^\dagger\}. \tag{11}$$

Here we calculate the integrated relaxation from all the excited states as our observables. This corresponds to the action signals from an excited state of interest. The method can be used to calculate all the possible action signals by defining appropriate relaxations. Action signals from three main transitions are calculated in this work. They are defined as

$$\text{Rel}_{10} = \int_0^{t_{\text{acquisition}}} dt\Gamma_{10}\text{Tr}\{\hat{L}_{\text{rel}}(1)\hat{\rho}_S(t)\hat{L}_{\text{rel}}^\dagger(1)\}, \tag{12}$$

$$\text{Rel}_{21} = \int_0^{t_{\text{acquisition}}} dt\Gamma_{21}\text{Tr}\{\hat{L}_{\text{rel}}(2)\hat{\rho}_S(t)\hat{L}_{\text{rel}}^\dagger(2)\}, \tag{13}$$

$$\text{Rel}_{32} = \int_0^{t_{\text{acquisition}}} dt\Gamma_{32}\text{Tr}\{\hat{L}_{\text{rel}}(3)\hat{\rho}_S(t)\hat{L}_{\text{rel}}^\dagger(3)\}, \tag{14}$$

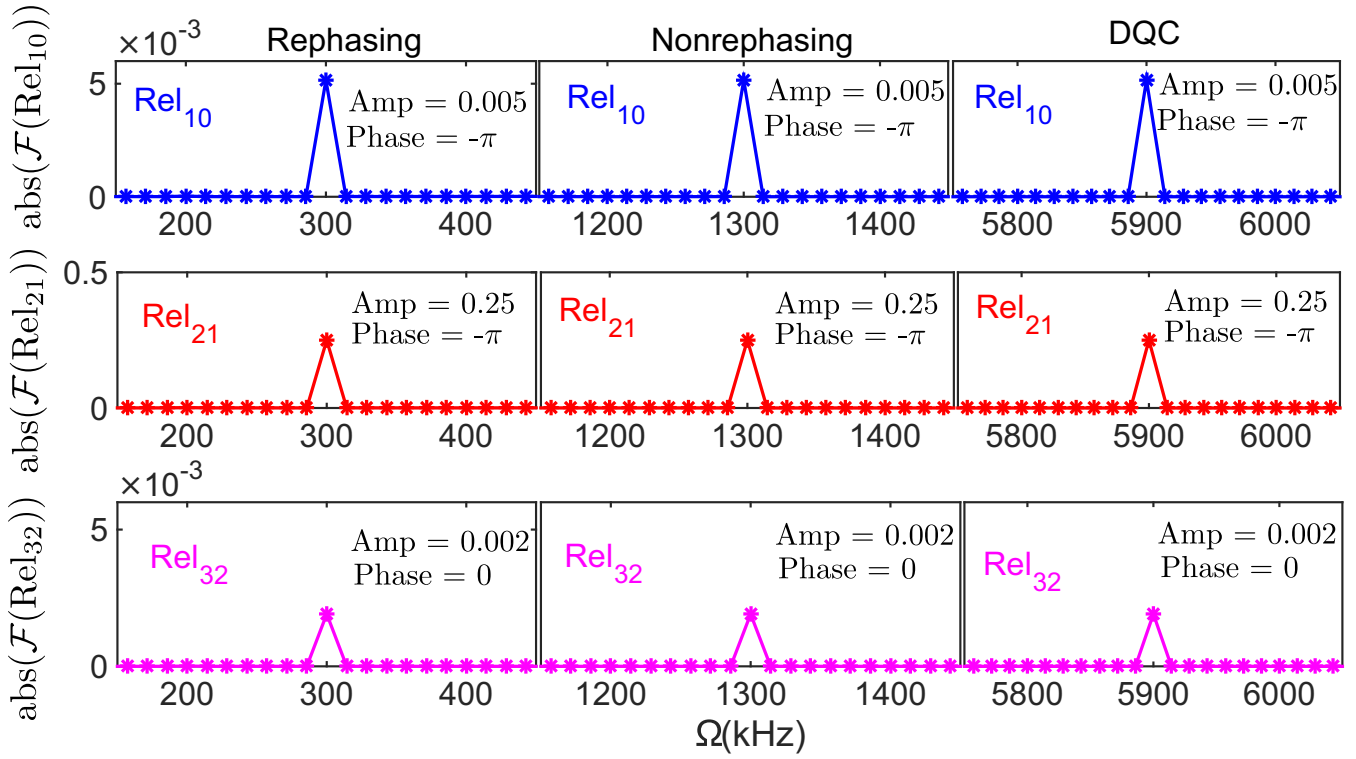

FIG. 3. Comparison of phases and amplitudes for the rephasing, nonrephasing, and DQC pathways for the observables Rel_{10}, Rel_{21}, and Rel_{32} at $T_1 = T_2 = T_3 = 0$. For better visibility, only the regions near the rephasing $\Omega = (\Omega_{43} - \Omega_{21})$, nonrephasing $\Omega = (\Omega_{43} + \Omega_{21})$, and double quantum coherence (DQC) $\Omega = \Omega_{42} + \Omega_{31} - \Omega_{41} + \Omega_{32}$ are plotted.

where Rel_{10} provides the action signal from the first excited state $|1\rangle$. This is the signal that is usually detected in the experiments as fluorescence. In addition, action signals from the higher excited states can be obtained from the other two observables Rel_{21} and Rel_{32} which provide signals from excited states $|2\rangle$ and $|3\rangle$, respectively. Although it is difficult to extract the signals from the higher excited states as fluorescence, their contribution can be important in experiments that detect photocurrent [33], photoelectrons or -ions [42,43].

C. Data collection

The integrated relaxation rates from all excited states as given in Eq. (12) are calculated by solving the density matrix in the Lindblad form. Here we use $t_{\mathrm{acquisition}} = 1.73$ ps. Together with $t_0 = 20$ fs, this ensures that all pulses are within the data acquisition window for all delays T_i chosen in this work. For each train of pulses the integrated signals are evaluated and recorded for many repeated excitations as a function of time ($t = mT$). m is varied from 0 to 5000 in order to acquire data for a time span of 70 μs, which is long enough to resolve all the relevant modulation components.

The signals oscillate at the linear and nonlinear combination of the modulation frequencies $\Omega_1, \Omega_2, \Omega_3, \Omega_4$. By Fourier transforming the action signal with respect to time ($t = mT$) at fixed interpulse time delays, the amplitude and the phase of the rephasing ($\Omega_{43} - \Omega_{21} = 300$ kHz), nonrephasing ($\Omega_{43} + \Omega_{21} = 1300$ kHz), and DQC at ($\Omega_{42} + \Omega_{31} = \Omega_{41} + \Omega_{32} = 5900$ kHz) signals are extracted.

Figure 3 shows the signals associated with the rephasing ($\Omega = 300$ kHz), nonrephasing ($\Omega = 1300$ kHz), and DQC ($\Omega = 5900$ kHz) at zero population time, $T_2 = 0$. The respective amplitudes and phases of the peaks are indicated within each plot. The amplitude for Rel_{21} is much larger than the relaxations Rel_{10} and Rel_{32}. This is a consequence of the assumed relaxation rates $\Gamma_{21} \gg \{\Gamma_{10}, \Gamma_{32}\}$ and a single relaxation pathway from $|3\rangle$ to $|2\rangle$. Here we also note that the phase of the population modulation in $|3\rangle$ is shifted by π with respect to the populations in $|2\rangle$ or $|1\rangle$. This will reflect in the 2D spectra obtained from the action signals originating from the different states as discussed below.

By repeating the above procedure with different time delays T_1 and T_3, a 2D signal can be constructed for the different population times T_2. Here we apply 30 steps with a spacing of 10 fs both for T_1 and T_3. The data are collected in the rotating frame with an angular frequency of 2.355 rad/fs. Two-dimensional Fourier transform of the time domain data (T_1, T_3) gives the desired complex valued 2D plot as a function of the excitation and the detection frequencies, respectively. Coherent dynamics and population transfer between excited states can be read off from the 2D maps. Corresponding double sided Feynman diagram can be constructed for further analyses of the dynamical processes.

IV. RESULTS

A. 2D spectra at $T_2 = 0$

For the model system shown in Fig. 2, the effect of excitation by a train of four phase modulated pulses as in

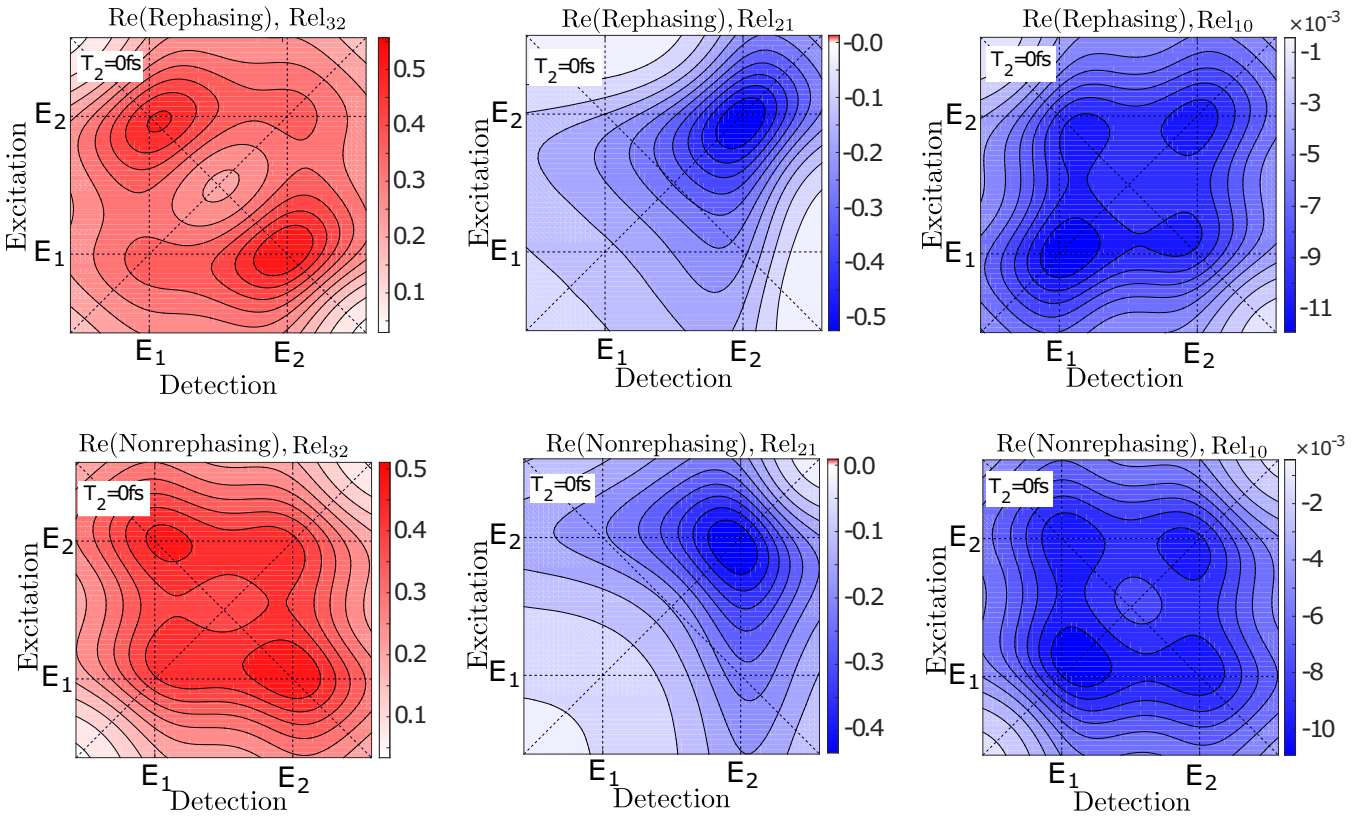

FIG. 4. The top row shows the real part of the rephasing signal from the different observables: Rel_{32}, Rel_{21}, and Rel_{10}. The bottom row shows the real part of the nonrephasing signals.

Eq. (1) is studied. The change in the system dynamics is carefully observed as a function of population time T_2 to study the population and coherence dynamics. The oscillatory signals due to coherent superpositions can be detected in such systems.

One of the advantages of our method is the ability to evaluate the action signals from the different allowed transitions. In the model considered, the three transitions $|3\rangle \rightarrow |2\rangle$, $|2\rangle \rightarrow |1\rangle$, and $|1\rangle \rightarrow |0\rangle$ can provide action signals Rel_{32}, Rel_{21}, and Rel_{10}, respectively. Note that Rel_{21} and Rel_{10} implicitly contain the contributions of the population relaxed from $|3\rangle$ to $|2\rangle$ and $|2\rangle$ to $|1\rangle$, respectively. Figure 4 shows the 2D action signals from Rel_{10}, Rel_{21}, and Rel_{32} at $T_2 = 0$. In each subplot, the energies for the two excitons with energy E_1 and E_2 are indicated by dashed line along the vertical and horizontal directions. The intersection of these lines give the diagonal and cross-peak positions visually. The spectra are grouped as rephasing (first row) and nonrephasing (second row). Usually, the rephasing and the nonrephasing spectra are summed in order to obtain the absorptive signal, which is also known as the total correlation [44–46].

We observe peaks at four positions in the 2D spectra, which are denoted according to the standard notation given in Fig. 5. The two peaks on the diagonal correspond to the two excitons at energy E_1 and E_2. These peaks are denoted as DP_1 and DP_2 in Fig. 5. The other two cross-diagonal peaks CP_{12} and CP_{21} are due to the correlations between the excitons at energies E_1 and E_2.

At population time $T_2 = 0$, the peaks in the rephasing signal in Fig. 4 are elongated along the diagonal while the nonrephasing peaks are elongated along the antidiagonal. This agrees well with the characteristic line shapes of the rephasing and the nonrephasing signals obtained by using perturbative techniques [2,47].

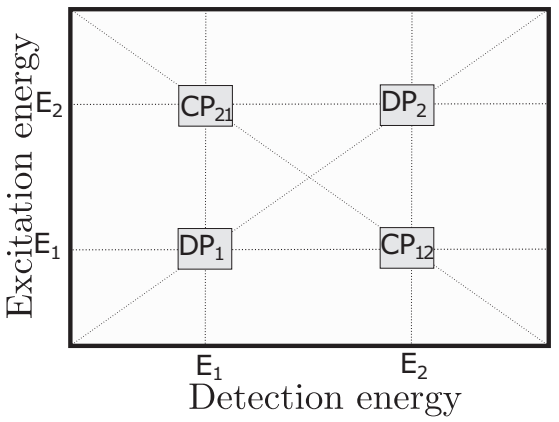

FIG. 5. Schematic diagram for the 2D spectrum of exciton model. The diagonal peak DP_1 is due to excitation and detection with a pulse energy E_1 and DP_2 is due to detection and excitation at energy E_2. Similarly the cross peaks: CP_{12} is observed by exciting at energy E_1 and detecting at a different energy E_2 while CP_{21} is observed by exciting at energy E_2 and detecting at energy E_1.

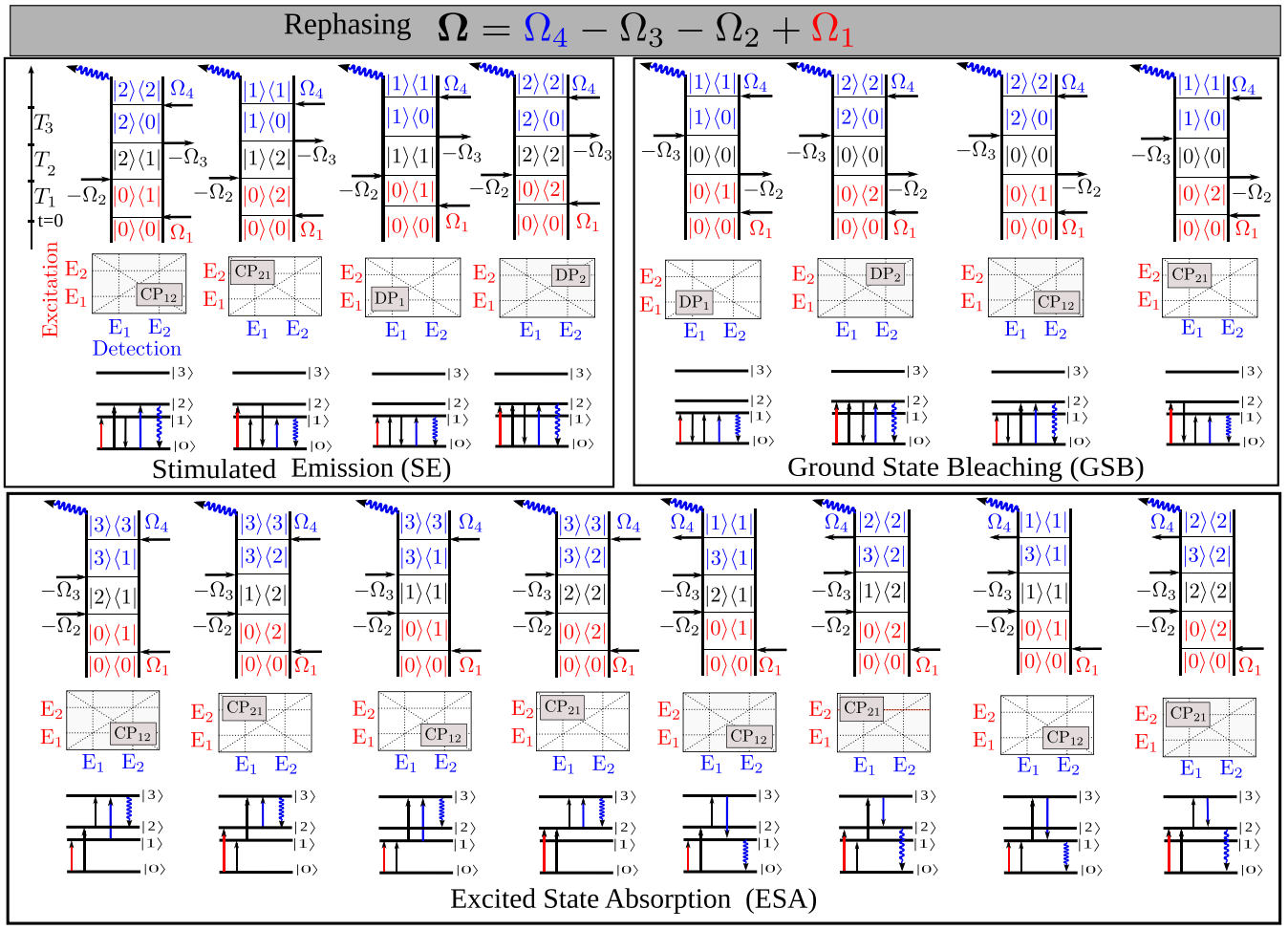

FIG. 6. All possible Feynman diagrams for the rephasing pathways.

The positions of the peaks in the different spectra in Fig. 4 can be related to the interaction pathways that contribute to the particular action signal. We illustrate the different pathways by using the double-sided Feynman diagrams in Fig. 6 and Fig. 7. In each figure (Figs. 6, 7, and 11), three different diagrams are shown for the different physical processes. The double-sided Feynman diagrams for each interaction pathways are shown on the top and the position of the peak that correspond to the pathways are shown in the middle. The action of the pulses on the system are shown in the bottom, where each arrow represents interaction with the field (half-transition) rather than the transfer of population. For the double-sided Feynman diagram, we use the common convention that an arrow pointing towards the ket or the bra side of the density matrix excites the system by acting on the ket or the bra of the density matrix, respectively [1]. Similarly, an arrow pointing outward from the ket or the bra of the density matrix de-excites the system by acting on the ket or the bra of the density matrix, respectively. In addition, we use the convention that an arrow pointing towards the left is represented by a positive phase Ω_j and an arrow pointing towards the right is represented by a negative phase $-\Omega_j$, where j is an index for the pulses. Since the double-sided Feynman diagrams are specific for the rephasing and the nonrephasing pathways, it is necessary to consider either the rephasing or the nonrephasing signals when explaining the positions and the amplitudes of peaks.

We first analyze the rephasing signal resulting from the third excited state Rel_{32}. As shown in Fig. 6, the signal arises due to ESA as this is the only process ending in the population of state $|3\rangle$. In order to differentiate it from the other ESA pathways that populate $|2\rangle$ and $|1\rangle$, this signal is also traditionally known as ESAII [48] (ESA pathways that populate $|1\rangle$ and $|2\rangle$ are designated as ESAI). There are four interaction pathways that contribute to ESAII, which generate two off-diagonal peaks at CP_{21} and CP_{12}, respectively. There are two minor peaks at DP_1 and DP_2 on the diagonal, which cannot be explained by the Feynman diagrams. These residual peaks result from the ambiguity in time ordering of the interactions during the overlap of the pulses, which mixes the rephasing and the nonrephasing signals. Such mixing of signals during the pulse overlap cannot be avoided in experiments. Here our method of direct simulation reveals such features, which can only be explained using Feynman diagrams for both the rephasing and the nonrephasing pathways. Generally, a 2D spectrum is the sum of the GSB, the SE, and the ESA signals. However, by choosing a proper action signal, such as molecular fragments from an energetic dissociative potential or photoelectrons, it would be feasible to isolate only the contributions from the ESA signal.

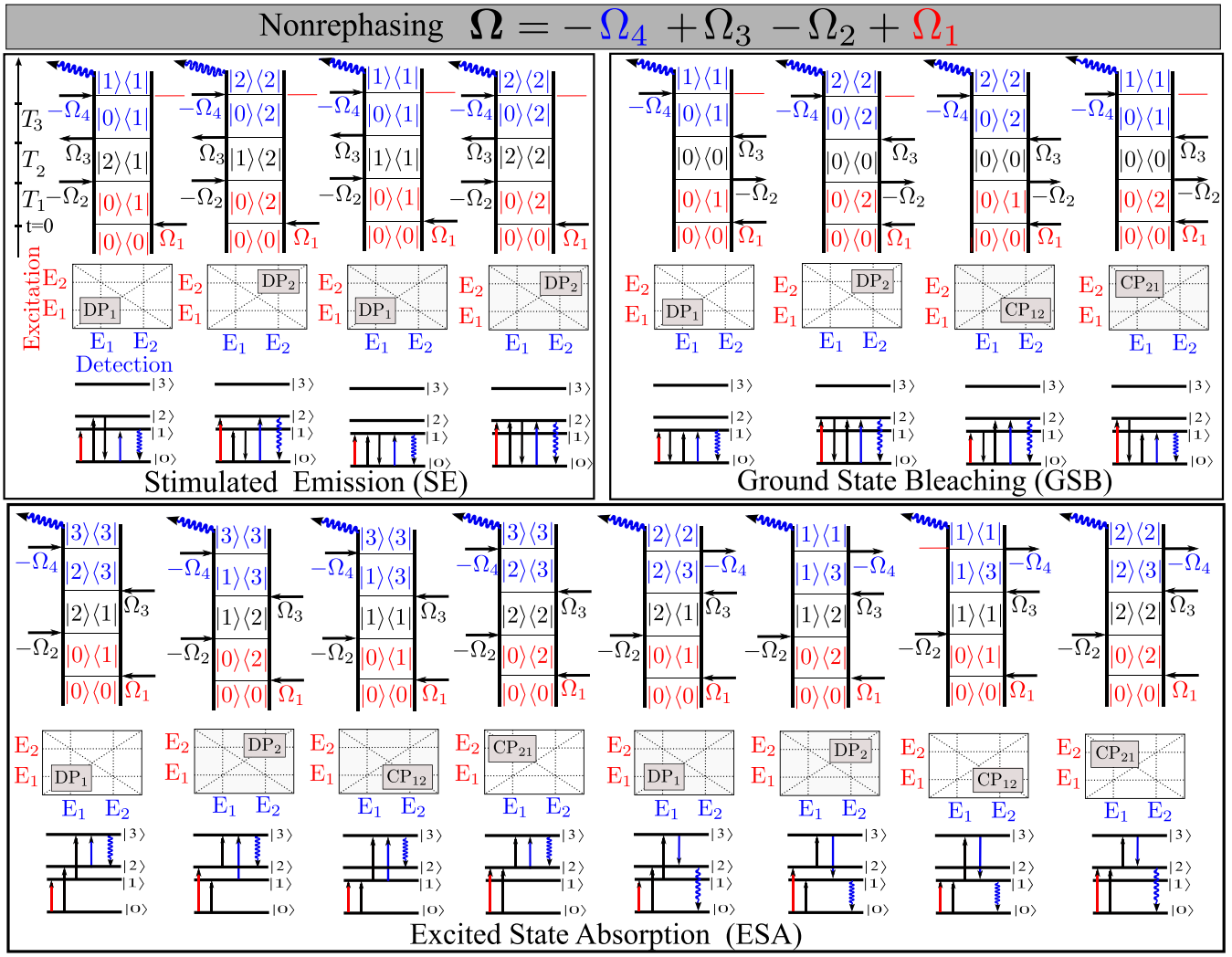

FIG. 7. All possible Feynman diagrams for the nonrephasing pathways.

Next, we analyze the 2D spectra obtained from Rel_{21}. There are six interaction pathways that populate $|2\rangle$ (Fig. 6); two each from the SE, the GSB, and the ESA. As the signals from the different pathways are additive, one expects peaks at CP_{12}, DP_2, and CP_{21}. However, the 2D spectra from the simulations show only one dominant peak at DP_2, which cannot be explained based only on the interactions that populate $|2\rangle$. In order to explain the results from the simulations, we also need to consider the relaxation processes that occur within $t_{\mathrm{acquisition}}$. $t_{\mathrm{acquisition}}$ in our simulations is 1.73 ps, which is significantly longer than the population relaxation from $|3\rangle$. Thus, Rel_{21} integrated over $t_{\mathrm{acquisition}}$ also contains the contributions from $|3\rangle$. However, when summing the contributions from the different states, one needs to take into account the phases of the modulations imparted on those states [33,48]. The relative phases of the modulations can be evaluated from the Feynman diagrams. We use the convention $\phi_{\mathrm{mod}} = \{\pi(-1)^{n_{\mathrm{Ib}}-1} - \pi\}/2$, where n_{Ib} is the number of interactions on the bra (or the ket) side of the density matrix. The phase of the modulations obtained from the simulations agree with the convention we use (see Fig. 3). A phase difference of π gives opposite sign to the signal. When the phases are taken into account, the contributions from $|3\rangle$ cancel the peaks at CP_{12} and CP_{21}, leaving only the diagonal peak at DP_2 in the 2D spectra obtained from Rel_{21}. Unlike in the rephasing spectra obtained from Rel_{32}, the mixing of rephasing and nonrephasing signal due to the ambiguity in time ordering during the pulse overlap does not generate any residual peaks because the cancellation of the off-diagonal peaks also occurs in the nonrephasing spectra (see the middle plot in the second row of Fig. 4). Here it is important to note that the cancellation of the off-diagonal peaks is complete only when the entire population in $|3\rangle$ relaxes to $|2\rangle$. This is not always the case in molecular or semiconductor excitonic systems in which other relaxation channels are present [49]. In such cases, it may be feasible to quantify the fraction of the population in $|3\rangle$ that relaxes to $|2\rangle$ from the residual off-diagonal peaks at CP_{12} and CP_{21}.

The rephasing 2D spectra obtained from Rel_{10} has four peaks at DP_1, DP_2, CP_{21}, and CP_{21}, which is similar to the spectra one expects from coherent signal detected 2D spectroscopy [4,6]. Nevertheless, it is important to discuss the origin of the four peaks in order to highlight the differences in the underlying interaction pathways. As shown in Fig. 6, there are six pathways that directly populate $|1\rangle$ due to the interaction

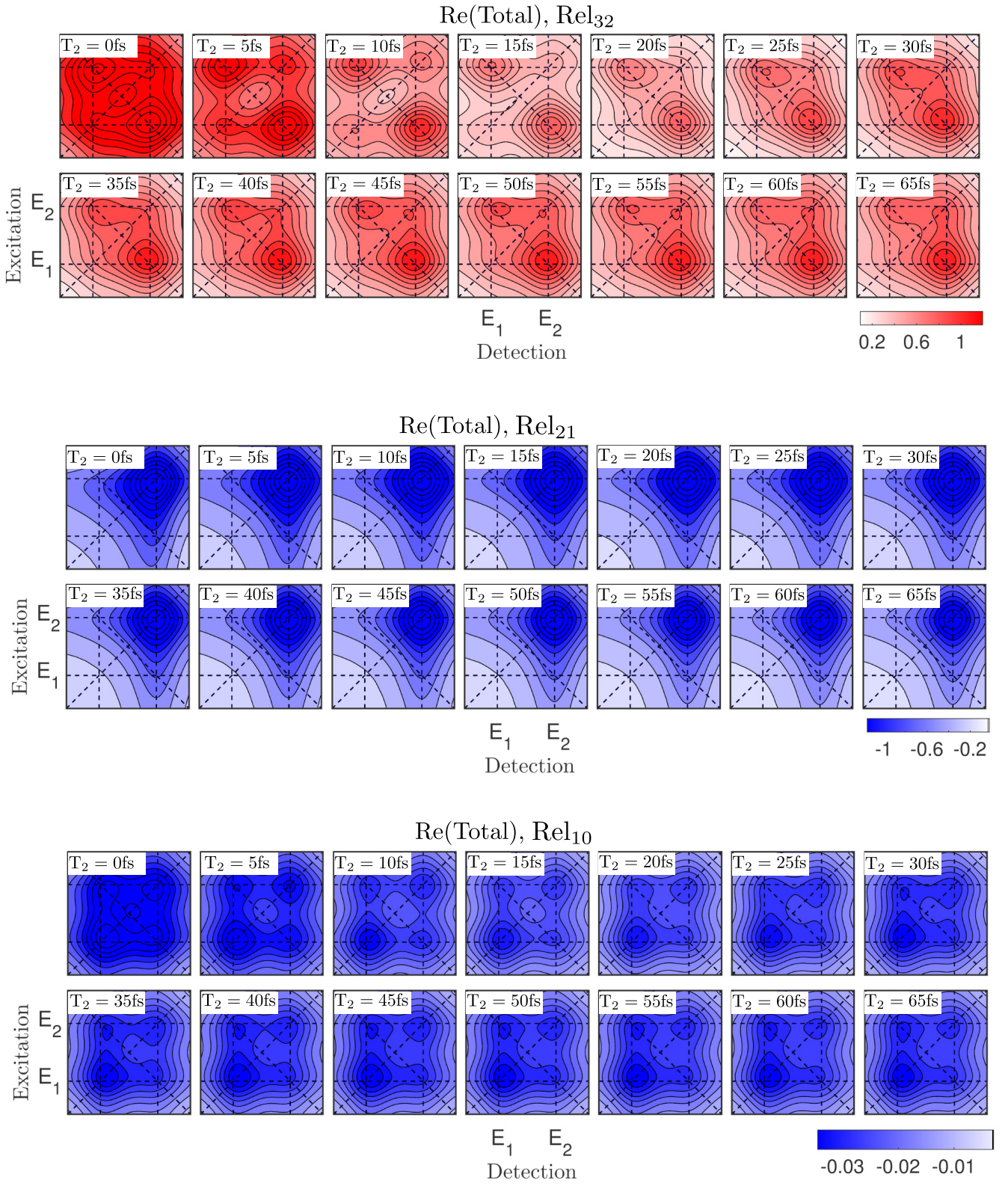

FIG. 8. Time evolution of the real part of the total correlation spectra obtained from the different action signals: Rel_{32} (top), Rel_{21} (middle), and Rel_{10} (bottom). The population time is varied by 5 fs from $T_2 = 0$. In each population time T_2 the spectrum is multiplied by the maximum amplitude of corresponding time domain data.

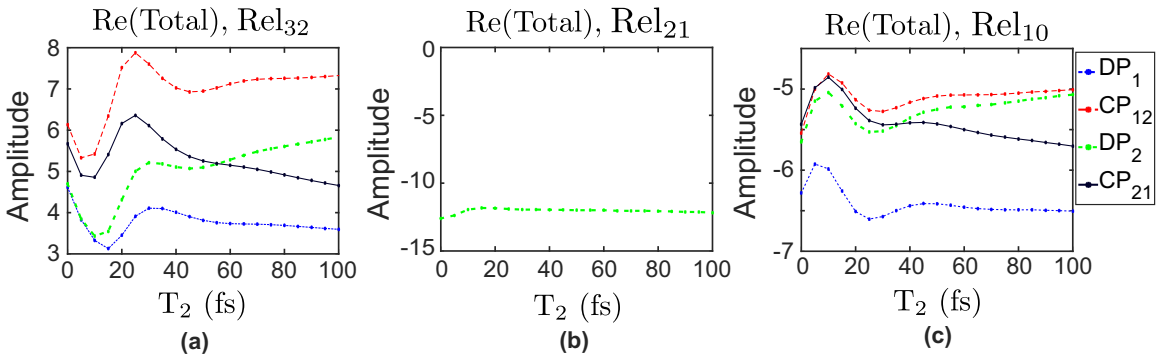

FIG. 9. Time evolution of the diagonal and cross peaks for the real value of the total correlation spectra.

of the four pulses, which generate three peaks at DP_1, CP_{12}, and CP_{21}. The fourth peak at DP_2 is due the relaxation of the population to $|1\rangle$. Even though all ESAI and ESAII pathways contribute to the signal detected from level $|1\rangle$, they are all off-diagonal. Furthermore, it is easy to see that because of the opposite phases, perfect pairwise cancellation of the ESAI and ESAII pathways takes place. Therefore, no ESA signal is visible in this detection. Thus, we conclude that the amplitude of the peak at DP_2 is a sensitive measure of the fraction of population that relax to $|1\rangle$ from higher excited states, which has been discussed previously [33,48].

The nonrephasing spectra at $T_2 = 0$ can be explained similarly based on the interaction pathways shown in Fig. 7. Nevertheless, the nonrephasing 2D spectra obtained from the signal Rel_{32} has four distinct peaks at CP_{12}, CP_{21}, DP_1, and DP_2. The nonrephasing 2D spectra obtained from the signals Rel_{21} and Rel_{10} have features similar to their rephasing counterparts.

B. Time evolution of the 2D spectra

In order to investigate the evolution with the population time T_2, we use the total correlation spectra. The total correlation spectra can also be easily measured in a pump-probe geometry [44–46], where the coherent response from the sample is heterodyned with the probe field. The total correlation spectra are important in quantifying the homogeneous and the inhomogeneous broadening. The inhomogeneous broadening produces line shapes elongated along the diagonal in the total correlation spectra [2,4,6,47]. The peaks in the calculated spectra are comparatively round mainly because the model does not include static disorder that leads to the inhomogeneous broadening.

The real part of the total correlation for the different actions signals at the various population times are plotted in Fig. 8. The energy splitting between the two excitons is

$$\Delta E = E_2 - E_1 = 1.55\,\text{eV} - 1.4855\,\text{eV} = 91.2\,\text{meV}.$$

The time steps for varying the population time T_2 is set to 5 fs.

We first analyze the evolution of the 2D spectra from the action signal Rel_{32}. The spectra at $T_2 = 0$ fs shows major cross peaks at CP_{12} and CP_{21}, and minor diagonal peaks at DP_1 and DP_2, which agree with the number of pathways that contribute to the peaks. In Figs. 7 and 6 we see that only one pathway contributes to each of the diagonal peaks while three pathways contribute to each of the off-diagonal peaks. In the pathways that generate the diagonal peaks, the system is in coherence between between $|1\rangle$ and $|2\rangle$ after the interaction with the first two pulses, which leads to the oscillation of the amplitudes of the peaks along T_2. Similarly, in two of the pathways that generate the off-diagonal peaks, the interaction with the first two pulses populate either $|1\rangle$ (peak at CP_{12}) or $|2\rangle$ (peak at CP_{21}), and the system is in coherence in one of the pathways. In general, one expects all the peaks to oscillate along T_2. In order to better quantify the beatings observed in Fig. 8, the peak values as a function of population time are plotted in Fig. 9(a). All the peaks DP_1, DP_2, CP_{12}, and CP_{21} in the total correlation spectra oscillate with similar frequency. The period of the oscillation is $T \approx 45$ fs, which matches the period $2\pi\hbar/(E_2 - E_1)$ of the beating frequency of the two excitons.

The 2D spectra from the signal Rel_{21} do not show clear oscillations with T_2 apart from the slight decrease in the

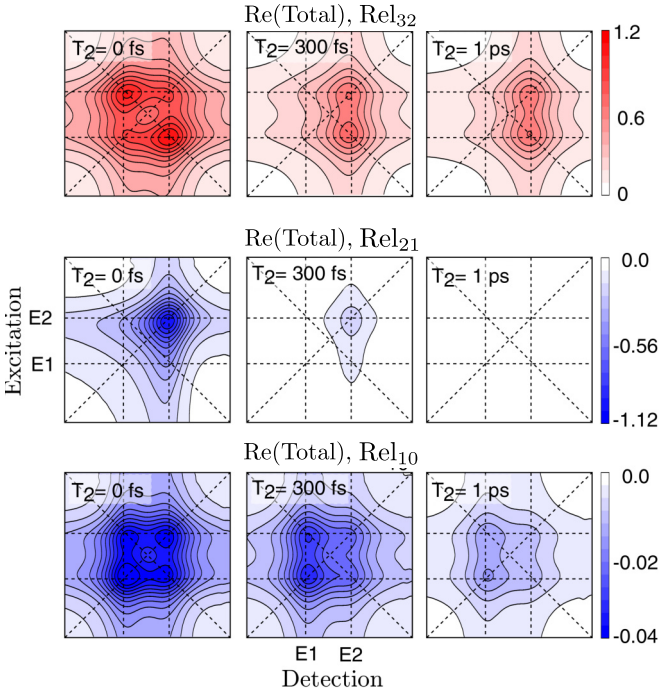

FIG. 10. Long-time evolution of the diagonal and cross peaks for the real value of the total correlation spectra.

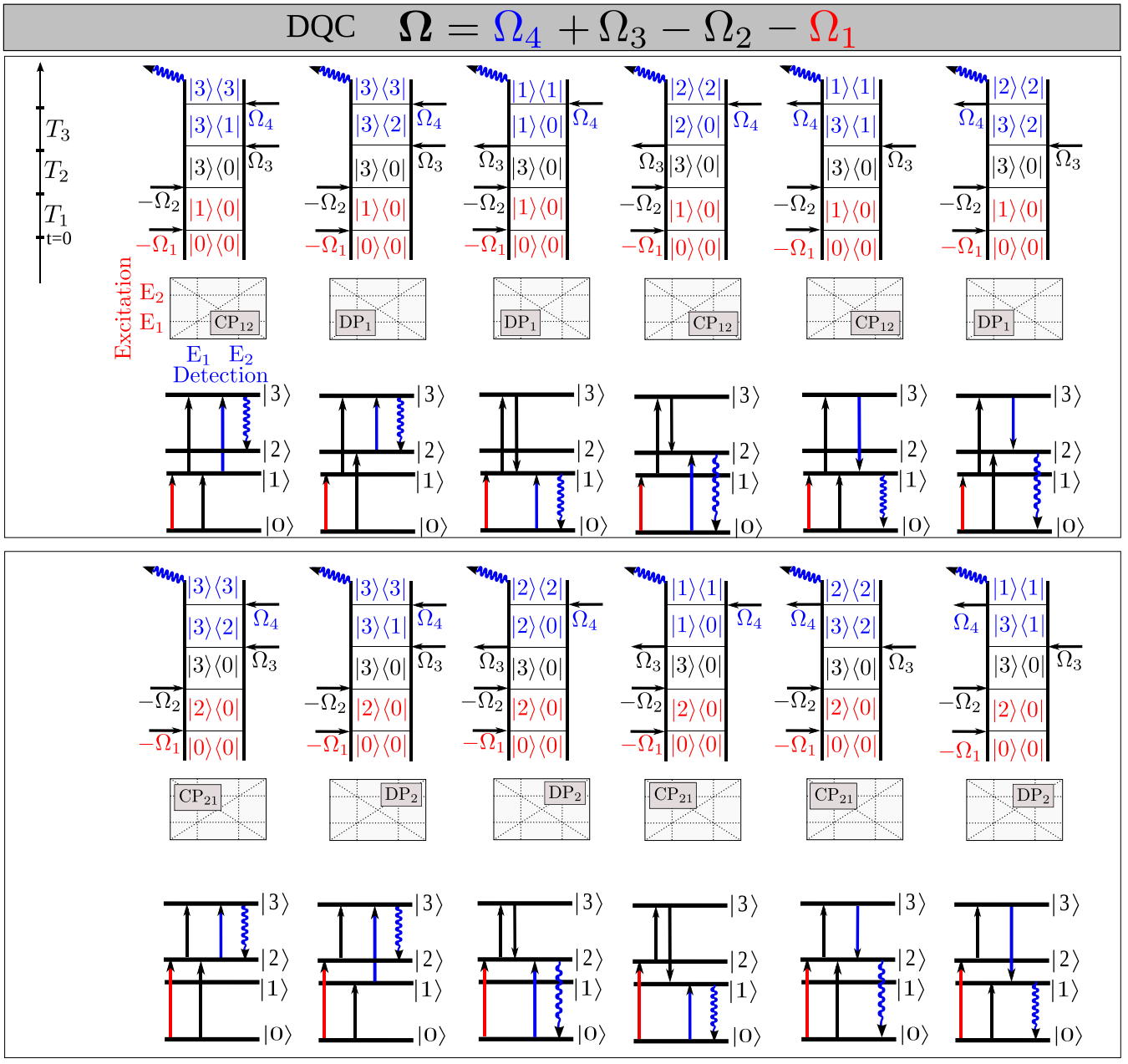

FIG. 11. All possible Feynman diagrams for the double quantum coherence (DQC) pathways.

initial times, which is due to the effects of pulse overlap. On the other hand, all the peaks in the 2D spectra from Rel_{10} show oscillations with a time period of 45 fs. As expected, the oscillations are opposite in phase with respect to the oscillations observed in the spectra obtained from Rel_{32}. The amplitude of the oscillations in Figs. 9(a) and 9(c) diminish rapidly mainly because of the short dephasing time of all the states used in the model (about 16 fs).

The relaxation of population from $|2\rangle$ to $|1\rangle$ can be observed in all the spectra. However, the evolution of the spectra are distinctly different for the different action signals. In the 2D spectra obtained from Rel_{32}, we observe a decrease in the amplitude of the signal at CP_{21} with a concomitant increase in the amplitude in the signal at DP_2. In the 2D spectra obtained from Rel_{21} the population relaxation from $|2\rangle$ to $|1\rangle$ reduces the amplitude of the signal at DP_2, which is the only peak in the spectra. Thus, when the relaxation is complete all the signal vanishes (see Fig. 10, middle row). Finally, the change in the amplitudes in the 2D spectra from Rel_{10} due to the relaxation of the population is similar to the ones expected in the coherent signal detected 2D spectroscopy [50]. The amplitude at DP_2 decreases with a concomitant increase in the amplitude at CP_{21} (see Fig. 10, bottom row). Thus, our calculations show that care should be taken when interpreting the population dynamics observed in the 2D spectra that are obtained from different action signals.

Next we analyze the signal from the DQC. Figure 11 shows all the pathways that contribute to the DQC signal. Note that in contrast to previous studies [40], we use the same notation and convention for the excitation axis as above. The DQC

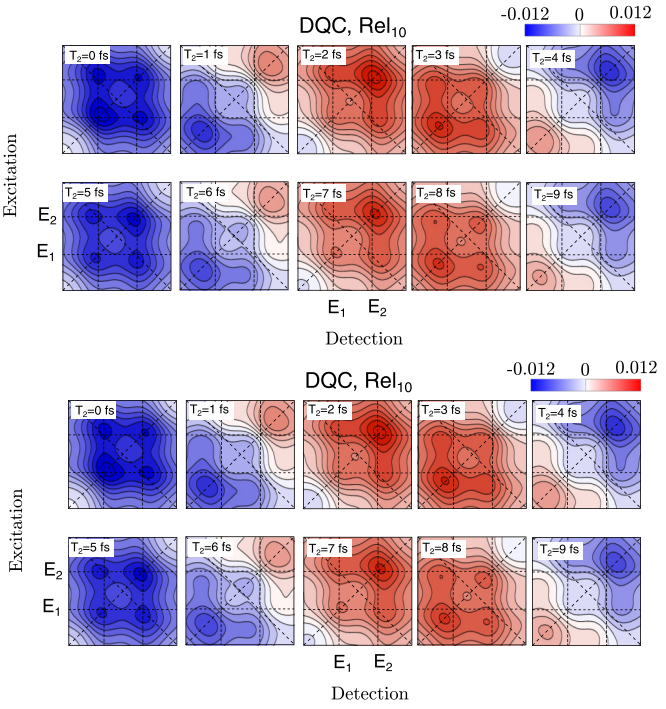

FIG. 12. Initial time evolution of the real part of the DQC spectra from the action signals Rel_{32} (top) and Rel_{10} (bottom).

spectra shown in Fig. 12 from the signals Rel_{32} and Rel_{10} at $T_2 = 0$ are similar to the corresponding nonrephasing spectra. Apart from the effects due to the pulse overlap, the signal Rel_{21} does not generate any DQC signal. This is because the signal Rel_{21} results from the sum of eight interaction pathways, out of which four originate from the population in $|3\rangle$ and the other four from the population in $|2\rangle$ (see Fig. 11). However, as the phase of the signals originating from $|3\rangle$ and $|2\rangle$ are opposite the signals cancel each other. The DQC spectra from Rel_{32} and Rel_{10} evolve rapidly with increasing T_2. Figure 12 show the evolution of the DQC spectra with a time step of 1 fs. The rapid evolution of the spectra is due to the coherence generated between the states $|0\rangle$ and $|3\rangle$ after the interaction of the system with the second pulse. Apart from the phase shift of π, the oscillations in both the spectra have a time period of about 1.4 fs, which matches the difference in the energy between states $|3\rangle$ and $|0\rangle$. Figure 13 shows the evolution of the amplitudes of the peaks at DP_1, DP_2, CP_{21}, and CP_{12} obtained from the DQC spectra for both signals Rel_{32} and Rel_{10} over longer population time. As shown in Fig. 13, the oscillations decay rapidly due to the loss of coherence between the states, which in the model is set to 16 fs. Thus, the results show that the DQC spectra, apart from providing the information about the electronic structure and the couplings between the excitonic states, also give additional insight into the dephasing rates of the high lying excited states in the system.

Actions signals, such as fluorescence and photocurrent, that have been used in experiments mainly originate from the population in S_1 [15,35]. Our results obtained from the signal Rel_{10} is relevant in understanding such experiments. Previous experiments were done on excitonic systems where the excitonic features were not clearly visible due to large background signals from the continuum of states in the semiconductors. In order to obtain distinguishable contributions from the different excitonic states as we have obtained from our simulations, it is important to investigate systems where the contribution from the continuum of the states is negligible. On the other hand, the simulations can also be extended by increasing the number of states in order to mimic the continuum of states in the semiconductors.

V. CONCLUSION

We have developed a method to calculate a 2D signal for an arbitrary quantum system using phase modulation technique. Clear signals enabling the study of time evolution for the different excited populations as a result of interaction with four laser pulses with distinct phase modulations have been obtained. We have shown that the method can be used to simulate the 2D spectra from action signals originating from different electronic states. In our simulation of a quantum system with coupled excitons, we observe fast coherent dynamics as well as slow relaxation processes. Moreover, the relaxation processes have different contributions to the 2D spectra obtained from different action signals. It also reveals extra diagonal peaks due to the overlap between the pulses

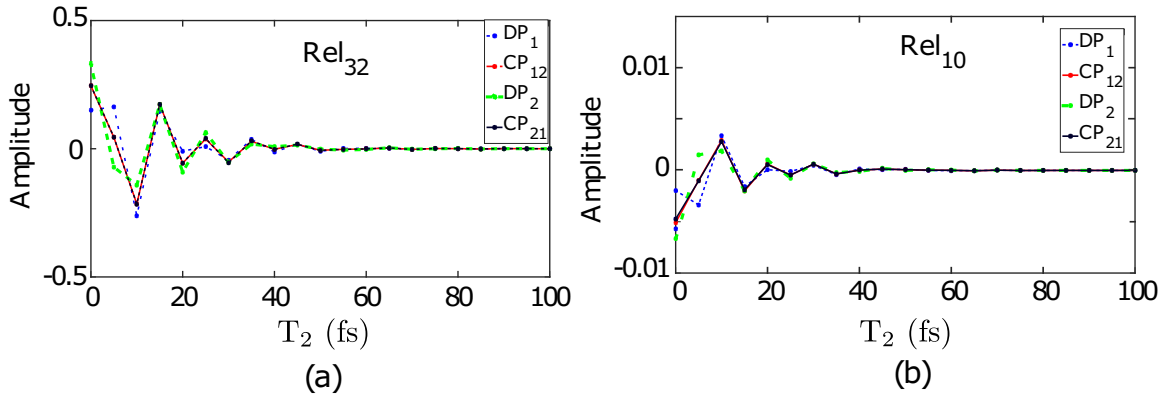

FIG. 13. Time evolution of the diagonal and cross peaks for the real part of the DQC spectra from the action signals Rel_{32} (left) and Rel_{10} (right). Note that due to lacking resolution of points the oscillation period appears much longer.

which are hardly avoidable in experiments. In addition, we have also shown that the technique can be used to study the dynamics of high lying excited states by using signals generated by multiple quantum coherences. In general, the technique can be used to simulate 2D spectra based on any action signal, such as fluorescence, photocurrent or photoions, originating from a quantum system. While we used a common four-level system here, which allowed for a direct comparison with a reasonable number of diagrams, the method is fully applicable to systems with a larger number of levels.

ACKNOWLEDGMENTS

We acknowledge the Swedish Research Council (VR), the Knut and Alice Wallenberg foundation (KAW), the Crafoord Foundation, and NanoLund for financial support.

[1] S. Mukamel, *Principles of Nonlinear Optical Spectroscopy* (Oxford University Press, New York, 1995), Vol. 29.
[2] P. Hamm and M. Zanni, *Concepts and Methods of 2D Infrared Spectroscopy* (Cambridge University Press, Cambridge, 2011).
[3] S. Mukamel, Annu. Rev. Phys. Chem. **51**, 691 (2000).
[4] M. Cho, Chem. Rev. **108**, 1331 (2008).
[5] S. M. G. Faeder and D. M. Jonas, J. Phys. Chem. A **103**, 10489 (1999).
[6] D. M. Jonas, Annu. Rev. Phys. Chem. **54**, 425 (2003).
[7] D. Egorova, M. F. Gelin, and W. Domcke, J. Chem. Phys. **126**, 074314 (2007).
[8] M. Cowan, J. Ogilvie, and R. Miller, Chem. Phys. Lett. **386**, 184 (2004).
[9] J. D. Hybl, A. W. Albrecht, S. M. G. Faeder, and D. M. Jonas, Chem. Phys. Lett. **297**, 307 (1998).
[10] J. D. Hybl, A. A. Ferro, and D. M. Jonas, J. Chem. Phys. **115**, 6606 (2001).
[11] T. Brixner, J. Stenger, H. M. Vaswani, M. Cho, R. E. Blankenship, and G. R. Fleming, Nature (London) **434**, 625 (2005).
[12] Y.-C. Cheng and G. R. Fleming, Annu. Rev. Phys. Chem. **60**, 241 (2009).
[13] T. Zhang, C. N. Borca, X. Li, and S. T. Cundiff, Opt. Express **13**, 7432 (2005).
[14] S. T. Cundiff, Opt. Express **16**, 4639 (2008).
[15] G. Nardin, T. M. Autry, K. L. Silverman, and S. T. Cundiff, Opt. Express **21**, 28617 (2013).
[16] J. Seibt and T. Pullerits, J. Phys. Chem. C **117**, 18728 (2013).
[17] V. Butkus, D. Zigmantas, L. Valkunas, and D. Abramavicius, Chem. Phys. Lett. **545**, 40 (2012).
[18] N. Christensson, H. F. Kauffmann, T. Pullerits, and T. Mančal, J. Phys. Chem. B **116**, 7449 (2012).
[19] D. Egorova, J. Chem. Phys. **140**, 034314 (2014).
[20] A. Ishizaki and G. R. Fleming, J. Phys. Chem. B **115**, 6227 (2011).
[21] T. Brixner, T. Mančal, I. V. Stiopkin, and G. R. Fleming, J. Chem. Phys. **121**, 4221 (2004).
[22] G. S. Schlau-Cohen, A. Ishizaki, and G. R. Fleming, Chem. Phys. **386**, 1 (2011).
[23] M. Cho, H. M. Vaswani, T. Brixner, J. Stenger, and G. R. Fleming, J. Phys. Chem. B **109**, 10542 (2005).
[24] D. Zigmantas, E. L. Read, T. Mančal, T. Brixner, A. T. Gardiner, R. J. Cogdell, and G. R. Fleming, Proc. Natl. Acad. Sci. USA **103**, 12672 (2006).
[25] B. K. Agarwalla, U. Harbola, W. Hua, Y. Zhang, and S. Mukamel, J. Chem. Phys. **142**, 212445 (2015).
[26] P. Tian, D. Keusters, Y. Suzaki, and W. S. Warren, Science **300**, 1553 (2003).
[27] A. K. De, D. Monahan, J. M. Dawlaty, and G. R. Fleming, J. Chem. Phys. **140**, 194201 (2014).
[28] Z. Zhang, K. L. Wells, E. W. J. Hyland, and H.-S. Tan, Chem. Phys. Lett. **550**, 156 (2012).
[29] H.-S. Tan, J. Chem. Phys. **129**, 124501 (2008).
[30] L. A. Pachón, A. H. Marcus, and A. Aspuru-Guzik, J. Chem. Phys. **142**, 212442 (2015).
[31] P. F. Tekavec, T. R. Dyke, and A. H. Marcus, J. Chem. Phys. **125**, 194303 (2006).
[32] P. F. Tekavec, G. A. Lott, and A. H. Marcus, J. Chem. Phys. **127**, 214307 (2007).
[33] K. J. Karki, J. R. Widom, J. Seibt, I. Moody, M. C. Lonergan, T. Pullerits, and A. H. Marcus, Nat. Commun. **5**, 5869 (2014).
[34] A. A. Bakulin, C. Silva, and E. Vella, J. Phys. Chem. Lett. **7**, 250 (2016).
[35] E. Vella, H. Li, P. Grégoire, S. M. Tuladhar, M. S. Vezie, S. Few, C. M. Bazán, J. Nelson, C. Silva-Acuña, and E. R. Bittner, Sci. Rep. **6**, 29437 (2016).
[36] V. A. Osipov, X. Shang, T. Hansen, T. Pullerits, and K. J. Karki, Phys. Rev. A **94**, 053845 (2016).
[37] K. J. Karki, L. Kringle, A. H. Marcus, and T. Pullerits, J. Opt. **18**, 015504 (2016).
[38] B. Brüggemann, P. Kjellberg, and T. Pullerits, Chem. Phys. Lett. **444**, 192 (2007).
[39] B. Brüggemann and T. Pullerits, New J. Phys. **13**, 025024 (2011).
[40] A. Nemeth, F. Milota, T. Mančal, T. Pullerits, J. Sperling, J. Hauer, H. F. Kauffmann, and N. Christensson, J. Chem. Phys. **133**, 094505 (2010).
[41] G. Lindblad, Commun. Math. Phys. **48**, 119 (1976).
[42] L. Bruder, M. Binz, and F. Stienkemeier, Phys. Rev. A **92**, 053412 (2015).
[43] L. Bruder, M. Mudrich, and F. Stienkemeier, Phys. Chem. Chem. Phys. **17**, 23877 (2015).
[44] L. P. DeFlores, R. A. Nicodemus, and A. Tokmakoff, Opt. Lett. **32**, 2966 (2007).
[45] E. M. Grumstrup, S.-H. Shim, M. A. Montgomery, N. H. Damrauer, and M. T. Zanni, Opt. Express **15**, 16681 (2007).
[46] M. Maiuri, J. Réhault, A.-M. Carey, K. Hacking, M. Garavelli, L. Lüer, D. Polli, R. J. Cogdell, and G. Cerullo, J. Chem. Phys. **142**, 212433 (2015).
[47] A. Tokmakoff, J. Phys. Chem. A **104**, 4247 (2000).
[48] A. Perdomo-Ortiz, J. R. Widom, G. A. Lott, A. Aspuru-Guzik, and A. H. Marcus, J. Phys. Chem. B **116**, 10757 (2012).
[49] W. A. Tisdale, K. J. Williams, B. A. Timp, D. J. Norris, E. S. Aydil, and X.-Y. Zhu, Science **328**, 1543 (2010).
[50] P. Kjellberg, B. Brüggemann, and T. Pullerits, Phys. Rev. B **74**, 024303 (2006).